ACS APPLIED MATERIALS & INTERFACES

www.acsami.org

Research Article

Temperature and Pressure Effects on Unrecoverable Voids in Li Metal Solid-State Batteries

Wahid Zaman, Le Zhao, Tobias Martin, Xin Zhang, Zhanjiang Wang, Q. Jane Wang, Stephen Harris, and Kelsey B. Hatzell*

Cite This: *ACS Appl. Mater. Interfaces* 2023, 15, 37401−37409

Read Online

ACCESS | Metrics & More | Article Recommendations | Supporting Information

ABSTRACT: All-solid-state batteries (ASSB) can potentially achieve high gravimetric and volumetric energy densities (900 Wh/L) if paired with a lithium metal anode and solid electrolyte. However, there is a lack in critical understanding about how to operate lithium metal cells at high capacities and minimize unwanted degradation mechanisms such as dendrites and voids. Herein, we investigate how pressure and temperature influence the formation and annihilation of unrecoverable voids in lithium metal upon stripping. Stack pressure and temperature are effective means to initiate creep-induced void filling and decrease charge transfer resistances. Applying stack pressure enables lithium to deform and creep below the yield stress during stripping at high current densities. Lithium creep is not sufficient to prevent cell shorting during plating. Three-electrode experiments were employed to probe the kinetic and morphological limitations that occur at the anode−solid electrolyte during high-capacity stripping (5 mAh/cm^2). The role of cathode−LLZO interface, which dictates cyclability and capacity retention in full cells, was also studied. This work elucidates the important role that temperature (external or *in situ* generated) has on reversible operation of solid-state batteries.

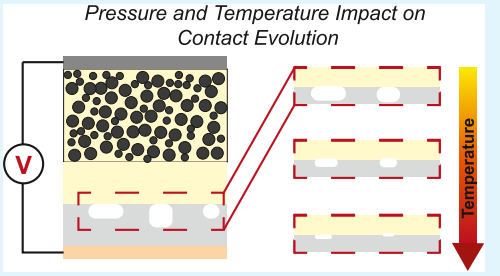

KEYWORDS: *Li metal, solid electrolyte, solid-state battery, contact mechanics, electrodeposition, electrodissolution*

INTRODUCTION

Li metal all-solid-state batteries are energy-dense alternatives to conventional lithium-ion batteries.[1] However, current lithium metal solid-state batteries suffer from low energy and power densities due to a range of instabilities that occur at lithium metal−solid electrolyte interfaces. Void or pore formation upon electrodissolution or stripping can lead to a decrease in interface contact area and increase in constriction resistance.[2−8] Increasing the stack pressure can increase the electrode−electrolyte contact area, decrease interfacial resistance and ensure void mitigation over cycling.[7,9] Computational and experimental work have recently shown that there is a critical stack pressure required for maintaining conformal contacts between Li−SE interfaces.[10−12] This also holds true for aqueous Li-ion batteries (< 500 kPa), but solid-state batteries generally require higher stack pressure (1−100 MPa).[13]

The optimum stack pressure depends on the solid electrolyte, current density, operating temperature, and the volume-changing properties in the subsequent cathode. For example, garnet oxide electrolytes ($Li_7La_3Zr_2O_{12}$) require a critical stack pressure of 3.4 MPa but are prone to mechanical fracture over 50 MPa. Sulfide electrolytes are softer and can withstand higher pressures (>100 MPa), but Li metal is prone to extrude through the electrolyte.[10,14] Within the optimum range, the creep behavior of Li metal is one of the most dominant factors in maintaining interfacial contact properties.[7] Li metal is viscoelastic with high volumetric strain and hence, stack pressure can facilitate Li creep under dynamic conditions.[15] This can effectively suppress voids, regulate Li dissolution kinetics and prevent plating-induced dendrites. At high current densities and high stripping capacities, the electro-chemomechanical behavior of Li metal significantly changes to form large vacancy accumulated regions. Hence, stress-assisted creep has to compete to annihilate the pores and prevent contact loss. The dynamic property of creep against current density significantly impacts Li stripping morphologies and cell shorting.

In this work, we studied the creep-induced properties in lithium metal solid-state batteries containing a garnet LLZO solid electrolyte. Specific focus was spent on understanding how plating and stripping dynamics are impacted in high-capacity operating modes (5 mAh/cm^2). Due to its intrinsic chemical stability against Li metal, LLZO is an excellent model system to evaluate the chemomechanics of Li metal. Prior reports showed that LLZO forms insulating surface carbonates (Li_2CO_3) in the air, which decreases its lithiophilicity. In this

Received: April 26, 2023
Accepted: July 4, 2023
Published: July 25, 2023

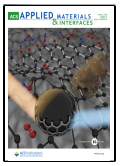

work, an O_2-assisted processing approach was employed to prepare carbonate-free LLZO which is readily wetted by Li metal upon contact.[16] After applying a stack pressure and subsequent melting of Li, a conformal contact with a resistance <5 Ω cm^2 can be achieved. We showed that the interfacial surface roughness (Li and LLZO), capacity, and current density significantly affect the morphological stability of Li during stripping, which indicates an enhanced void growth due to vacancy accumulation. We demonstrated that applying stack pressure is an effective method to enable stripping at high current densities due to the high creep rate. However, stack pressure alone cannot mitigate and solve for unrecoverable voids which form during the first stripping cycle. We explore how operation at elevated temperatures can improve the reversible operation of high-capacity lithium metal solid-state batteries.[17,18] Combining pressure and temperature can significantly improve the chemomechanics of Li to enable stable and long-term cycling. Utilization of *in situ* generated heat may provide a way for lithium metal to self-repair under full cell operating conditions.

EXPERIMENTAL SECTION

LLZO Solid Electrolyte. Ta-doped $Li_7La_3Zr_2O_{12}$ solid electrolyte was prepared by ball milling the precursors. LiOH was pre-dried at 200 °C for 6 h, and La_2O_3 was pre-dried at 900 °C for 10 h. The two prior precursors were mixed with ZrO_2 and Ta_2O_5 in the stoichiometric ratio. Anhydrous isopropanol was used as the milling solvent. The ball milling was carried out in a Pulverisette premium 7 ball mill for 4 h at a rotation speed of 500 rpm. The mixer was then dried under air for solvent evaporation and collected via sieving. The precursor powder was then annealed at 900 °C for 8 h in air. Another round of ball milling was carried out to reduce the particle size (350 rpm, for 2 h). The powder was then pelletized by using a pellet die under 300 MPa for 15 min. For the symmetric and full cell studies, a pellet die of 10 mm diameter was used. For the 3-electrode setup, a pellet die of 20 mm diameter was used. The pellets were then covered with additional LLZO (mother powder) and sintered under O_2 flow at 1235 °C for 8 h. After sintering, the pellets were cleaned and wet polished with sandpapers to ensure a smooth surface. The final pellets have a relative density of 95−96% and thickness of around 1.5 mm. After polishing, the pellets were immediately transferred to an Ar-filled glove box to avoid Li_2CO_3 growth on the surface.

Cell Assembly. Lithium foils were punched into 4 mm diameter electrodes and attached to the LLZO surface at 2 MPa. Copper foil was pressed on top of Li foil as the current collector. To ensure negligible interfacial contact resistance, the Li−LLZO assembly was heated up to 250 °C for 30 min. The symmetric cells were cycled in a pressure cell setup (Figure S1a−c). A custom designed 3-electrode setup made of PEEK was utilized for stripping and plating experiments. A small Li metal disk (2 mm diameter) was used as the reference electrode in the 3-electrode setup. The Li disk was attached to a copper rod and inserted into the PEEK chamber.

All full cells utilized the $LiFePO_4$ (LFP) cathode active material. The composite cathode included LFP, conducting carbon (super P), PVDF binder, and LiTFSi salt with a weight ratio of 55:10:10:25. *N*-methyl-2-pyrrolidone (NMP) was used as the solvent. The wet slurry was cast on a carbon-coated aluminum foil and dried at 100 °C for 24 h to remove the solvent. Cathode disks (4 mm diameter) were punched from the dry film and attached to LLZO by applying 10 MPa of pressure. Both symmetric and full cell assemblies were then placed inside a modified pressure cell setup where the stack pressure was applied with a compressing jig. A compression load cell (Omega Engineering) was used to monitor the stack pressure. To avoid cell relaxation over time, a stainless steel spring was attached to the compression jig.

Materials and Electrochemical Characterization. X-ray diffraction (XRD) was carried out on LLZO powders and pellets in Rigaku Smart Lab (Cu Kα X-ray). The diffraction patterns were taken from 10 to 50° with 0.01° step size. Potentiostatic electrochemical impedance spectroscopy (PEIS) was carried out using Biologic SP300 (maximum frequency 7 MHz) and VMP3 (maximum frequency 1 MHz) potentiostats. The lowest frequencies for symmetric and full cells were 1 Hz (SP300) and 100 mHz (VMP3) with an amplitude of 50 mV. Electrochemical impedance spectroscopy was also carried out to measure the ionic conductivity of sintered LLZO pellets. The impedance spectra was fitted using RelaxIS software. Cycling profiles for the symmetric and full cells were conducted under a galvanostatic current. Full cells with a LFP composite cathode were cycled between 2.5 and 4 V. Cyclic voltammetry (CV) measurements were carried out on full cells with a scan rate of 0.1 mV/s.

Surface Profiling. Surface mapping of LLZO was carried out on a laser scanning confocal microscope (Olympus OLS5000) with a 50× objective lens. The map resolution was 0.25 μm (x and y) and 0.0008 μm in the z-direction. To obtain comprehensive images, data from 9 scans were stitched together to construct each image. This process resulted in a total measurement area of 715 × 715 μm^2 per image. Line profiles of surface roughness were examined with the instrument's software package to get an initial understanding of the surface topography. The height data from the image was saved as .csv files for more detailed topography analysis.

Computational Modeling. A three-dimensional (3D) contact model was built to simulate the Li−LLZO interface while exposed to an applied stack pressure. The model considers the LLZO surface roughness, lithium metal deformation, and lithium creep based on the methods reported in the following references.[7,12,19] A representative computational domain of 400 μm × 400 μm is selected for contact analysis. The contact conditions are

$$\int_{\Gamma} p(x, y)\mathrm{d}\Gamma = P \cdot A_{\mathrm{geo\_Li}} \tag{1}$$

$$p(x, y) > 0,\ \mathrm{gap}(x, y) = 0;\ (x, y) \notin \Gamma$$
$$p(x, y) = 0,\ \mathrm{gap}(x, y) > 0;\ (x, y) \subset \Gamma \tag{2}$$

$$\mathrm{gap}(x, y) = -u_z(x, y) + h_{\mathrm{LLZO}}(x, y) - h_{\mathrm{Li-creep}}(x, y) - \delta_r \tag{3}$$

where $p(x,y)$ is the normal pressure distribution on the Li surface, Γ is the contact region, P is the average stack pressure, $A_{\mathrm{geo\_Li}}$ is the geometric area of the Li surface, gap(x,y) is the interfacial gap between Li and LLZO, $u_z(x,y)$ is the normal elastoplastic deformation of Li, h_{LLZO} is the surface roughness of LLZO, $h_{\mathrm{Li-creep}}(x,y)$ is the height reduction due to Li creep, and δ_r is the rigid-body approach. The conjugate gradient method (CGM)[20] and the continuous convolution fast Fourier transform CC-FFT algorithm were implemented in this approach[21−23] to solve the contact problem in eqs 1−3.

Area Specific Resistance Calculation. The interface resistance can be determined by[7]

$$R_{\mathrm{int}} = \frac{\mathrm{ASR}}{A_c} \tag{4}$$

where ASR is the area specific resistance between the solid electrolyte and lithium metal anode and A_c is the projected contact area between the electrolyte and electrode.[24] The area specific resistance between the anode and the solid electrolyte can be monitored during electrochemical stripping and plating experiments. The area specific resistance is initially small because the solid electrolyte is polished prior to stripping experiments, and lithium is melted directly to the solid−electrolyte interface. Surface contamination and roughness can impact continuous contact between the lithium metal and solid electrolyte and increase the area specific resistance of a cell. The surface roughness of LLZO in this study is about R_q = 0.8 μm (Figures S2 and S3). Based on the material parameters (elastic modulus, Poisson's ratio, yield strength) (Table S1) and the experimental data, the ASR value was estimated to be around 15 ± 0.5 Ω cm^2. The contact area maps are shown in Figure S7. Figure S8

https://doi.org/10.1021/acsami.3c05886
ACS Appl. Mater. Interfaces 2023, 15, 37401−37409

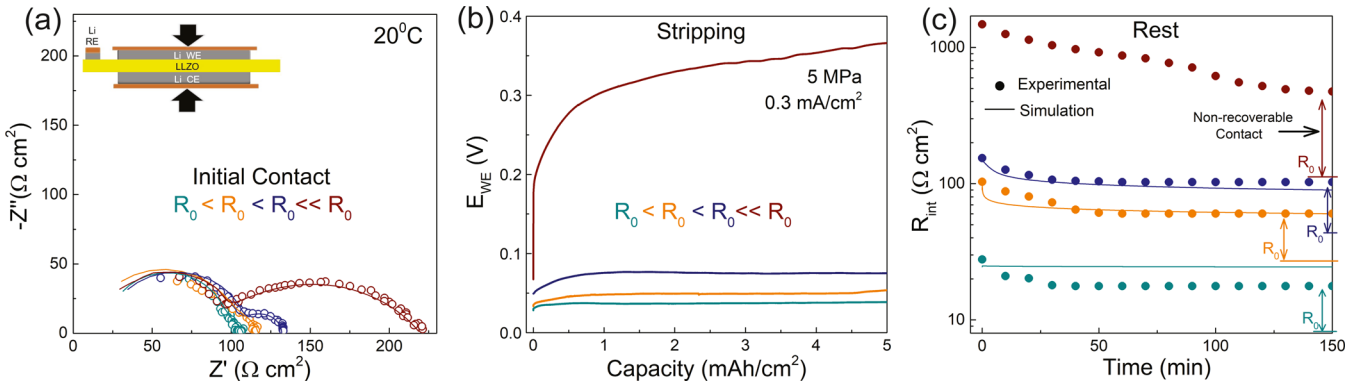

Figure 1. Nyquist plots showing the interfacial resistance of the working electrode (stripping) for four different symmetric cells (a). Stripping profiles of the symmetric cells (b) and change in interfacial resistances due to Li creep (c). Solid lines represent simulated resistances.

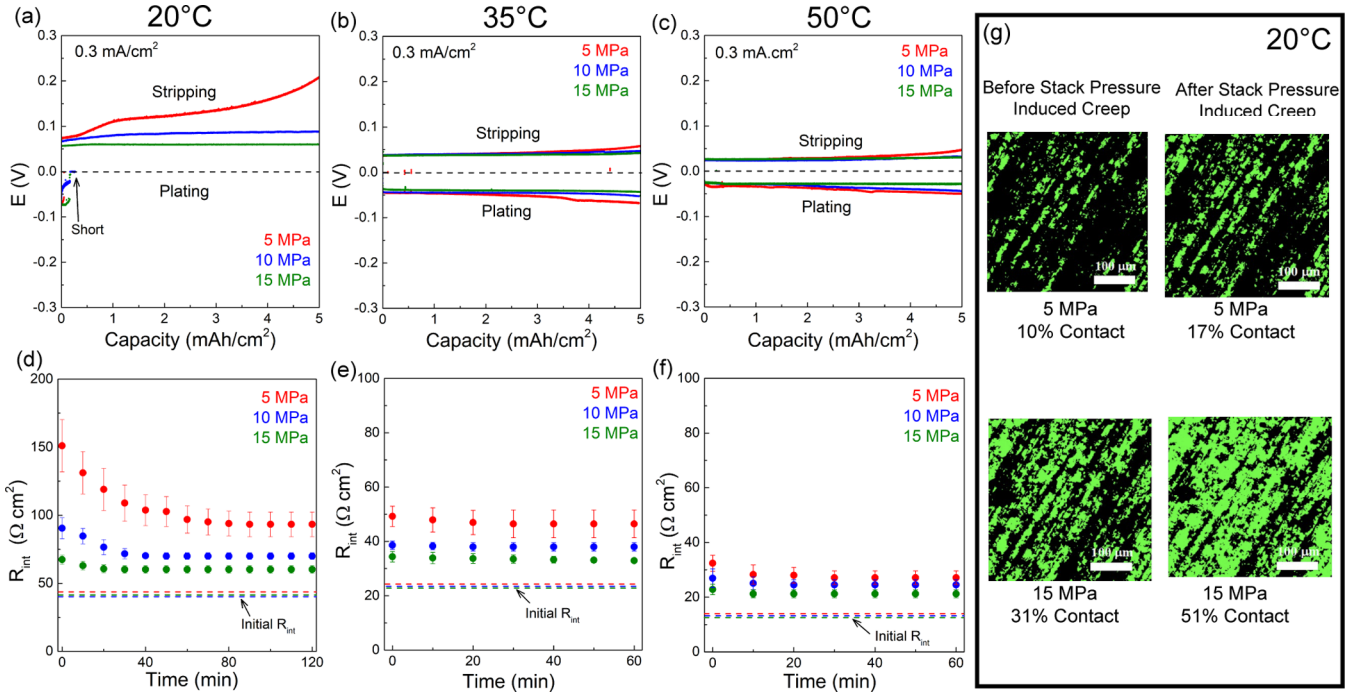

Figure 2. Stripping and plating profile of a Li−LLZO−Li symmetric cell (2-electrode) at 5, 10, and 15 MPa at (a) 20 °C, (b) 35 °C, and (c) 50 °C. Change in the interfacial resistance due to Li creep (during post-stripping hold) at (d) 20 °C, (e) 35 °C, and (f) 50 °C. Error bars represent an average of 3 experiments. (g) Contact maps of surfaces before and after creep at 5 and 15 MPa for 2 h.

shows how contact area changes at 5 MPa and 60 °C for each cell stripped in Figure 1a.

Li Creep. The indentation rate, $\dot{\epsilon}_{i\_creep}$, for the lithium creep law can be expressed as follows:

$$\dot{\epsilon}_{i\_creep}(x, y) = \frac{\dot{h}_{i\_creep}(x, y)}{u_{Li}(x, y)} \quad (5)$$

where $u_{Li}(x,y)$ is the lithium normal elastoplastic deformation, $\dot{\epsilon}_{i\_creep}$ is zero in the noncontact regions, and $\dot{h}_{i\_creep}$ is the height reduction rate due to lithium creep. The height reduction can be determined from the experimental data[7,15,25] with the following relationship:

$$\dot{h}_{i\_creep}(x, y) = C_r\left[\frac{p(x, y)}{\sigma_Y}\right]^m \exp\left(\frac{-Q_c}{RT}\right)\cdot u_{Li}(x, y) \quad (6)$$

where C_r is a material constant, Q_c is the creep activation energy, R is the gas constant, and m is the stress exponent at T = 298 K. The values for m and $C_r \exp(-Q_c/RT)$ are influenced by the thickness of the Li metal.[5,26] The experimental data assumed m = 12 and $C_r \exp(-Q_c/RT) = 4.5 \times 10^{-8}$ MPa^{-12} s^{-1}.

RESULTS AND DISCUSSION

High-Capacity Utilization of Lithium Metal and Initial Contact. The initial interfacial resistance R_{int} (or contact resistance) of Li−LLZO generally depends on a few critical parameters: surface contamination of Li and LLZO, the presence of Kirkendall voids, and existence of delamination regions.[27] All LLZO pellets in this study were prepared under O_2, and thus the initial interfacial resistance (R_{int}) is likely due to incomplete contact between the anode and solid electrolyte. Lithium metal exhibits creep-induced deformation under stack pressure which can potentially depress the voids. The deformation is considered purely plastic and driven by the dislocation glide of Li from the bulk region to the interface. To avoid high creep-induced strain, we used Li foils with thicknesses between ≈80 and 100 μm. These films only undergo <3% of strain at 15 MPa.[5] Lithium can form a nearly permanent contact with LLZO even after pressure is removed because it is highly adhesive. The surface of the lithium anode

https://doi.org/10.1021/acsami.3c05886
ACS Appl. Mater. Interfaces 2023, 15, 37401−37409

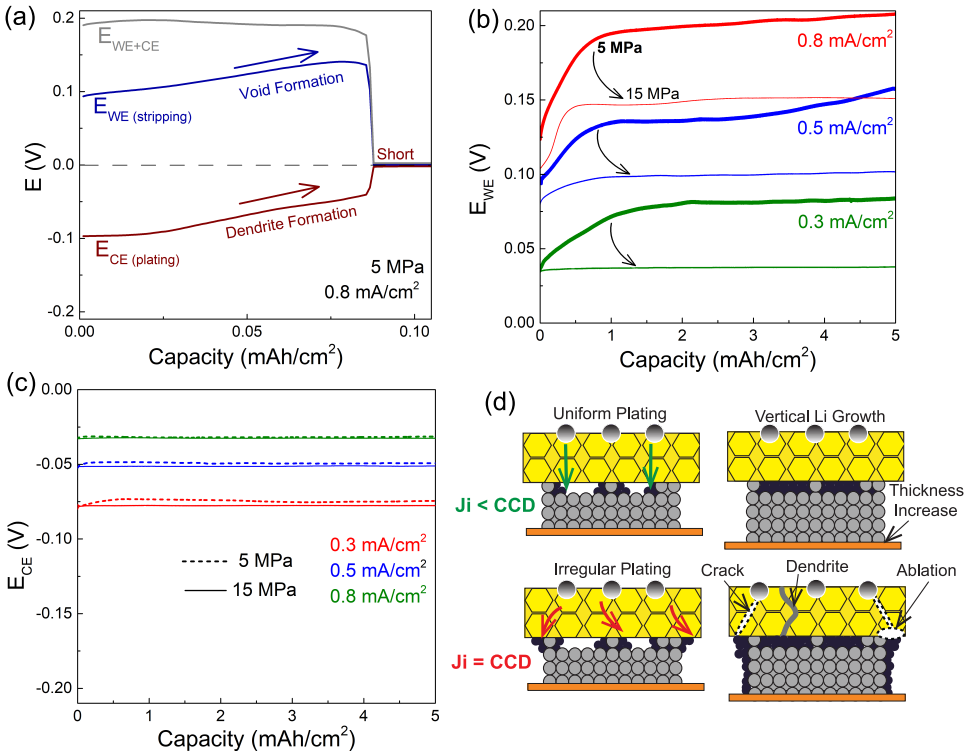

Figure 3. Stripping and plating profiles of a symmetric cell with high contact resistance, showing the plating-induced shorting at 0.8 mA/cm^2 in a 3-electrode setup. The stripping side has a negligible impact on cell shorting (a). Li stripping profiles (working electrode) at the current density of 0.3, 0.5, and 0.8 mA/cm^2 (b). Li plating profiles (counter electrode) at the current density of 0.3, 0.5, and 0.8 mA/cm^2. Stack pressure was 5 and 15 MPa (c). Schematic of Li plating mechanism at low and high current densities (J_i), displaying the effects of irregular and isolated Li deposition on LLZO. Figures to the right of original figure are after a period of time (d).

becomes rough and the electrode−electrolyte contact area decreases upon stripping.[28] The bulk lithium also experiences morphological changes due to the increased number of vacancies.[29] These phenomena get worse at high current densities. Theoretical and experimental studies suggest that Li creep is a dominant mechanism for the void annihilation and restabilization of the interfaces.[16,30] We observed a correlation between initial R_{int} and lithium metal relaxation at the electrolyte surface (Figure 1a,c). We assembled four different cells with varying degrees of interfacial resistance (e.g., contact area) (R_0 = 2, 13, 30, and 120 Ω cm^2). Each cell was cycled at 0.3 mA/cm^2, 5 MPa, and 5 mAh/cm^2 (thickness ≈25 μm). The cell with R_0 of 120 Ω cm^2 displayed a high degree of polarization (>300 mV) after the Li dissolution process, whereas the cell with R_0 of 2 Ω cm^2 showed limited polarization (Figure 1b). The cells were then rested for over 2 h, during which EIS was conducted intermittently. Lithium creep was more visible in the cells assembled with a high initial interfacial resistance. Li creep improves the interfacial contact by filling up the voids (from 1600 to 500 Ω·cm^2). The creep effect was minimal in the cells with smaller R_0 and almost negligible for R_0 of 2 Ω cm^2 (Figure 1c).

High-Capacity Utilization of Lithium Metal and Operating Temperature. High per-cycle areal capacities (≈5 mAh/cm^2) are necessary for adoption of lithium metal solid-state batteries. External operating conditions, including applied pressure and temperature, can influence the reversible operation of lithium metal batteries. A symmetric Li−Li cell at 20 °C can strip ≈5 mAh/cm^2 of lithium metal at 5, 10, and 15 MPa against a garnet LLZO solid electrolyte (Figure 2a). No polarization was observed in cells held at 10 and 15 MPa and cells held at elevateed temperatures 50 °C. Significant polarization was observed in the cell held at 5 MPa and 20 °C. Increases in cell polarization during stripping is a signal of severe void formation or large changes in contact area at either or both of the lithium electrodes. Each cell (e.g., 5, 10, and 15 MPa) at 20 °C immediately shorts upon reversing the direction of the current flow. Cells held at slightly elevated temperatures around 35 and 50 °C demonstrated reversible high per-cycle capacities and low overpotentials that were independent of operating pressure (Figure 2b,c).

Void formation and loss of electrode contact are common after high-capacity stripping. Lithium creep was monitored using electrochemical impedance spectroscopy after stripping 5 mAh/cm^2 capacity (Figure 2d−f). In the absence of an electric field (no electrical current), we can directly monitor changes in the contact surface area as a result of lithium diffusion and creep as a function of pressure and temperature. Lithium metal is viscoelastic and should deform and experience creep dynamics when there is an applied stack pressure. At the atomic scale, Li creep drastically reduces the dislocation density and diffusion barriers between Li vacancies and adatoms.[31] Cells exposed to high stack pressures will have more dislocations and thus experience a greater adatom diffusion to the interface and void filling. Stack pressure can improve overall contact resistance. Despite the potential improvement with an applied pressure, all cells only demonstrated limited improvement in the interfacial resistance over time when held at a elevated stack pressure.

The horizontal dashed lines in Figure 2d−f are the initial native state prior to stripping, and the markers represent impedance measurements taken during a 2-h resting period.

https://doi.org/10.1021/acsami.3c05886
ACS Appl. Mater. Interfaces 2023, 15, 37401−37409

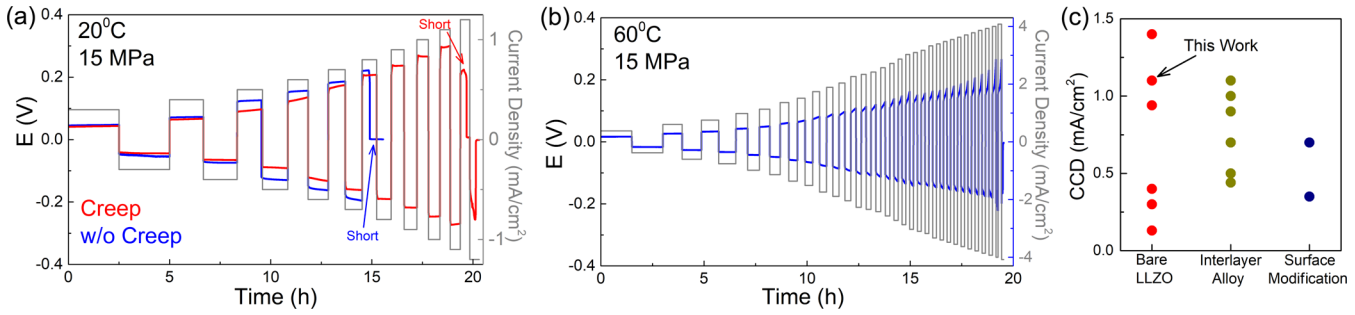

Figure 4. Attainable critical current density (CCD) for LLZO at 20 °C with and without creep protocol (a) CCD of LLZO at 60 °C (b). Comparison of room-temperature (20−25 °C) critical current densities (CCD) reported for Li metal and LLZO. "Bare LLZO" represents CCD of Li−LLZO without any interlayer or surface alterations.[35−39] "Interlayers/Alloys" represents CCD, where a thin interlayer or alloying mechanism was used to increase the wettability.[40−46] "Interlayers/Alloys" represents CCD where the surface structure of LLZO was modified by patterning[47,48] (c).

The interfacial resistance was almost identical for all cells held at different pressures and the same temperature. Overall the interfacial resistance decreased from around 50 Ω cm^2 at 20 °C (Figure 2d) to 12 Ω cm^2 at 50 °C (Figure 2f). The largest change in the interfacial resistance was observed for the cells with 5 mAh/cm^2 capacity stripped at 5 MPa and 20 °C. These cells experienced a nearly 3× increase in the interfacial resistance to 150 Ω cm^2. After static holding, the interfacial resistance decreased to 100 Ω cm^2 (Figure 2d). The interface resistance increased universally for all cells. Lithium has an low yield stress (σ_{Li} = 16 MPa)[12,32] which suggests that the lithium either forms unfavorable and nonuniform morphologies (e.g., nano- or microstructure) and/or has contamination which makes it unable to recover its initial form at all pressures and temperatures studied. The electrode−electrolyte contact area was modeled using the contact model. Interfaces with high interfacial resistances see an increase in the contact area from 10 to 17% while holding an applied stack pressure as low as 5 MPa. Holding the cell at an elevated pressure resulted in an improvement in the contact area from 31 to 51% after high-capacity stripping and stack pressure holding protocol (Figure 2g). Stack pressure can induce lithium creep and aid in improving the contact area between the anode and solid electrolyte. However, these improvements are limited. All cells across all pressures and temperatures could not achieve the original contact area before stripping, suggesting that there are unrecoverable voids formed during the first stripping cycle. Because of the high dependence of the creep rate on stress, the creep rate slows down dramatically with time as the peak contact stresses are relieved. Thus, getting back to the original contact area would take an inordinate amount of time. Balancing stripping and plating mechanisms with an intercalation reaction is critical for overcoming these dynamics that cause irreversible harm.

High-Capacity Stripping Impact on Li Plating and Dendrite-Induced Shorting. Symmetric cells will have stripping and plating occur at the same time but different electrodes (working and counter). Lithium stripping creates unrecoverable voids which may drive increasing overpotentials and hot spots for degradation. Lithium deposition can result in the formation and growth of lithium filaments and dendrites. The underpotential during the plating process is related to the initiation of Li nuclei ($Li^+ + e^- \rightarrow Li^0$) on the Li metal anode. Previous reports have shown that Li prefers to nucleate at surface irregularities at the LLZO surface.[33] The size, shape, and density of Li nuclei depends on the current density and temperature. The thickness of the bulk Li grows during electrodeposition. This expansion or growth of lithium metal can induce stress points (hydrostatic) which lead to irregular lithium growth (filament, whiskers, etc.). This instability can induce cell shorting. To examine the effects of high-capacity lithium metal utilization on both the stripping and plating, we assembled a 3-electrode experiment (Figure 3a). A quick drop of plating voltage often means a dendrite has formed. It is unlikely that the stripping process has any influence on this mechanism. We also observed that, if the current is reversed before the voltage drops down to ≈0 V, the dendrite can be pushed back, and this prevents shorting. Stack pressure-induced Li creep has limited impact on the plating electrode. The stripping overpotential increases with increasing current density and decreasing pressure which confirms our initial observations (Figure 3b). Pressure has less of an impact on the overpotential when examining the plating electrode response (Figure 3c). At low plating current densities (e.g., $J_i \ll$ CCD), there is a slow growth of lithium metal at the plating electrode which can improve the uniformity of the film (Figure 3d). In contrast, high current densities (e.g., J_i = CCD) can lead to (i) uncontrolled and irregular Li growth (vertical and lateral), (ii) mechanical failure of electrolyte (ablations and cracks), and (iii) increase in interfacial electronic properties (Figure 3c). These degradation mechanisms were not observed on the stripping electrode. Instead a dark red shade of few microns was observed on the stripping side (Figure S10). The origin of this dark red is either from corrosion with the current collector or reactions with nitrogen and trace contaminants. Lithium contamination comes in many forms and is highly dependent on working environment and lithium source. Overall pressure and current density have a greater impact on the morphology of the stripping electrode than the plating electrode.

Lithium Metal Creep and Critical Current Density. To understand the impact that lithium metal creep has on the critical current density, we ran two types of CCD tests. The first was a conventional constant capacity CCD test, while the second had periods of hold to facilitate creep before increasing the current. The cells with the lithium creep protocol experienced a 15 min rest step at 15 MPa before increasing the current. This stabilization step can induce lithium metal creep and restabilize the interface. All cells had excess lithium metal (25 mAh/cm^2) and cycled 1 mAh/cm^2 during each cycle. At room temperature, the critical current density was around 0.6 mA/cm^2. The cell with the creep protocol experience a significantly higher CCD of 1.1 mA/cm^2 (Figure

https://doi.org/10.1021/acsami.3c05886
ACS Appl. Mater. Interfaces 2023, 15, 37401−37409

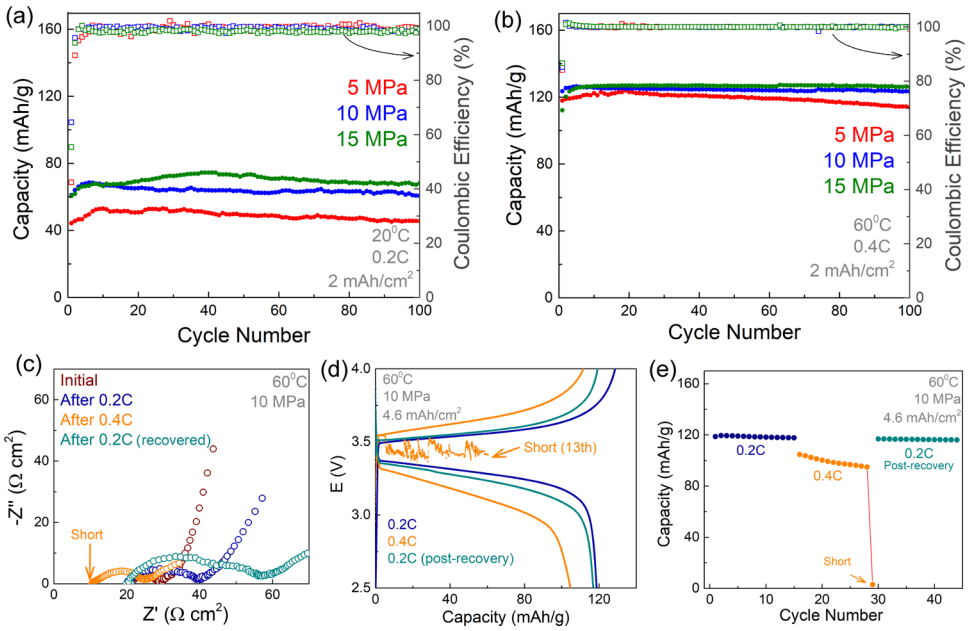

Figure 5. Stack pressure dependent cycling performance of a Li−LLZO−LFP full cell at 5, 10, and 15 MPa at (a) 0.2C, 20 °C, and (b) 0.4C, 60 °C. The areal capacity of the cathode was 2 mAh/cm^2. (c) Cell resistance evolution of Li−LLZO−LFP full cells with thicker cathode (4.6 mAh/cm^2 areal capacity) after cycling at 0.2C and 0.4C. (d) Galvanostatic charge/discharge profiles at high current density showing cell failure at 0.4C at 13th cycle and subsequent recovery after slow discharging (0.1C). (e) Cycling performance of the cell at 0.2C and 0.4C. Operating temperature was 60 °C and stack pressure was 10 MPa.

4a). This is noticeably higher than what frequently has been reported in the literature (Figure 4c). However, it should be noted that a higher critical current density (>6 mA/cm^2) has been demonstrated but while cycling less lithium per cycle.[34] The effect of high stack pressure and subsequent creep (due to resting) is evident from the EIS measurements as they showed almost no increase in interfacial resistances. Generally, high critical current densities in the LLZO cell is achieved by the introduction of a lithiophilic interlayer (Au, In, ZnO) to increase the Li wettability (Figure 4c). In this work, we show how lithium creep can influence the CCD. This observation is more obvious at elevated temperature 60 °C. The CCD was greater than 4 mA/cm^2 at 60 °C due to a substantially higher creep rate (Figure 4b). We also looked at the stripping limit of LLZO where Li can be stripped up to 2.4 mA/cm^2 at 20 °C without shorting (e.g., critical stripping current density, $CCD_{stripping}$) (Figure S9). Stack pressure-induced deformation (static and transient) enables greater stability in lithium metal electrodissolution at higher current densities. However, reversal of the current in the deposition step is dependent on the contact between the stripping electrode and solid electrolyte.

Reversible Operation of High-Capacity Lithium in Full Cells. Often void and filament formation in lithium metal is studied in model symmetric or three-electrode cells. These experiments do not fully capture the dynamics that would happen in a full cell where the cathode may undergo a zero-, positive-, or negative volume change. To examine the role of stack pressure on performance, we assembled full cells with a $LiFePO_4$ (LFP) composite cathode. LFP shows very small volume change upon lithiation/delithiation and is chemically stable against LLZO. Two operating conditions were considered: 0.2C at 20 °C and 0.4C at 60 °C (Figures 5a,b, S14, and S15). Both operating conditions showed a low Coloumbic efficiency of (<70% for 20 °C and <90% for 60 °C in the 1st discharging cycle). Increasing the stack pressures increases the capacity for all cells held at 20 °C (Figure 5a). At elevated temperatures, the capacity of the full cells are improved by 50%, but the capacity appears to be independent of the applied pressure (Figure 5b). While the discharge capacity is 30−43% less than the theoretical capacity (170 mAh/g), the capacity retention was excellent over 100 cycles (Figure 5b).

Thin, low areal capacity cathodes do not mimic the current density regimes that are common with short-circuiting. To examine critical current density regimes, we assembled high-capacity composite cathodes with areal capacities around ≈4.6 mAh/cm^2 at 60 °C. Increasing the capacity leads to absolute current densities of ≈1.8 mA/cm^2 at 0.4C. At 0.2C (current density 0.9 mA/cm^2), the cell delivered a capacity of 117 mAh/g with excellent retention (Figure 5d). The cell polarization increases and capacity decreases when C-rate increases (Figures 5d and S16). The discharge capacity gradually decreased from 105 to 95 mAh/g within 12 cycles, and a short-circuiting occurred during the 13th cycle. The capacity decline and sudden shorting of the full cell can be attributed to the dendrite formation-growth phenomena which is similar to what we observed in symmetric cells. Similar shorting in full cells for high areal loading was reported for sulfide electrolytes with NMC cathodes, but the electrochemical signature for shorting in LLZO is different.[49] The cell resistance decreases and electrochemical impedances moves to the left after shorting (Figure 5c). The cell was recovered by discharging the cell at 0.1C. EIS before and after the slow discharge demonstrates how the cell goes from shorted to unshorted (Figure 5c). The ability to revive a cell, post short, is commonly observed in symmetric cells when lithium creates a bridge between each electrode. Li metal can be reduced to the anode ($Li^+ + e^- \rightarrow Li$). This provides additional insights into the role Li−LLZO interface plays in a full cell. Despite the

https://doi.org/10.1021/acsami.3c05886
ACS Appl. Mater. Interfaces 2023, 15, 37401−37409

unwanted increase in cell resistance, the formation of CEI layer does not drastically affect the cell performance (Figure S14). However, upon further cycling at a high C-rate, high anodic interfacial voids and irregular plating can decrease the lifetime of the battery. Similar to symmetric cells, full cells also require an optimum stack pressure (>10 MPa) to maintain a stable Li−LLZO interface.

CONCLUSIONS

High-capacity utilization of lithium metal is critical for achieving high energy density solid-state batteries that can displace conventional batteries. There are several notable challenges that need to be overcome to achieve reversible operation of 5 mAh/cm^2 capacity of lithium metal. First, most studies work with excess lithium metal to avoid irregular and nonuniform stripping and plating dynamics. The latter is likely highly dependent on cell geometry and adhesion between components. The second challenge is the formation of voids at the anode interface upon electrodissolution. Voiding can create local hot spots that drive high current densities and premature failure. Herein, we show that stack pressure is not enough to overcome these unrecoverable voids and becomes less important when pairing lithium metal with a volume-changing cathode. Thermal treatment provides *a* potentially faster and more reliable way to heal voids and improving the overall reversibility of *a* lithium metal anode. More work is needed to understand how intrinsic thermal properties (e.g., thermal gradients, joule heating, etc.) can be implemented to reduce the presence of unrecoverable voids in high-capacity lithium metal anodes.

ASSOCIATED CONTENT

Supporting Information

The Supporting Information is available free of charge at https://pubs.acs.org/doi/10.1021/acsami.3c05886.

Experimental details and testing architectures for evaluating lithium metal; three-dimensional surface maps and table of modeling parameters; and contact maps and electrochemical characterization (PDF)

AUTHOR INFORMATION

Corresponding Author

Kelsey B. Hatzell − *Department of Mechanical and Aerospace Engineering, Princeton University, Princeton, New Jersey 08540, United States; Andlinger Center for Energy and Environment, Princeton University, Princeton, New Jersey 37240, United States;* orcid.org/0000-0002-5222-7288; Email: kelsey.hatzell@princeton.edu

Authors

Wahid Zaman − *Department of Mechanical and Aerospace Engineering, Princeton University, Princeton, New Jersey 08540, United States; Department of Mechanical Engineering, Vanderbilt University, Nashville, Tennessee 37240, United States*

Le Zhao − *Department of Mechanical Engineering, Northwestern University, Evanston, Illinois 60208, United States; Institute of Tribology Research, Southwest Jiaotong University, Chengdu 610031 Sichuan, China*

Tobias Martin − *Department of Mechanical Engineering, Northwestern University, Evanston, Illinois 60208, United States*

Xin Zhang − *Department of Mechanical Engineering, Northwestern University, Evanston, Illinois 60208, United States;* orcid.org/0000-0001-6668-0289

Zhanjiang Wang − *Institute of Tribology Research, Southwest Jiaotong University, Chengdu 610031 Sichuan, China*

Q. Jane Wang − *Department of Mechanical Engineering, Northwestern University, Evanston, Illinois 60208, United States*

Stephen Harris − *Lawrence Berkeley National Laboratory, Berkeley, California 94720, United States*

Complete contact information is available at: https://pubs.acs.org/10.1021/acsami.3c05886

Notes

The authors declare no competing financial interest.

ACKNOWLEDGMENTS

This material is based upon research supported by the Office of Naval Research under Award Number N00014-22-1-2406S. K.B.H. and W.Z. acknowledge support from the National Science Foundation 2041505 and 2140472. S.J.H was supported by the Laboratory Directed Research and Development Program of Lawrence Berkeley National Laboratory under U.S. Department of Energy contract no. DE-AC02-05CH11231.

REFERENCES

(1) Hatzell, K. B.; Chen, X. C.; Cobb, C. L.; Dasgupta, N. P.; Dixit, M. B.; Marbella, L. E.; McDowell, M. T.; Mukherjee, P. P.; Verma, A.; Viswanathan, V.; Westover, A.; Zeier, W. G. Challenges in Lithium Metal Anodes for Solid-State Batteries. *ACS Energy Lett.* **2020**, *5*, 922−934.

(2) Eckhardt, J. K.; Klar, P. J.; Janek, J.; Heiliger, C. Interplay of dynamic constriction and interface morphology between reversible metal anode and solid electrolyte in solid state batteries. *ACS Appl. Mater. Interfaces* **2022**, *14*, 35545−35554.

(3) Fleig, J.; Maier, J. The impedance of imperfect electrode contacts on solid electrolytes. *Solid State Ionics* **1996**, *85*, 17−24.

(4) Feng, M.; Yang, C.-T.; Qi, Y. The Critical Stack Pressure to Alter Void Generation at Li/Solid-Electrolyte Interfaces during Stripping. *J. Electrochem. Soc.* **2022**, *169*, No. 090526.

(5) Haslam, C. G.; Wolfenstine, J. B.; Sakamoto, J. The effect of aspect ratio on the mechanical behavior of Li metal in solid-state cells. *J. Power Sources* **2022**, *520*, No. 230831.

(6) Wang, M. J.; Choudhury, R.; Sakamoto, J. Characterizing the Li-solid-electrolyte interface dynamics as a function of stack pressure and current density. *Joule* **2019**, *3*, 2165−2178.

(7) Zhang, X.; Wang, Q. J.; Harrison, K. L.; Roberts, S. A.; Harris, S. J. Pressure-driven interface evolution in solid-state lithium metal batteries. *Cell Rep. Phys. Sci.* **2020**, *1*, No. 100012.

(8) McConohy, G.; Xu, X.; Cui, T.; Barks, E.; Wang, S.; Kaeli, E.; Melamed, C.; Gu, X. W.; Chueh, W. C. Mechanical regulation of lithium intrusion probability in garnet solid electrolytes. *Nat. Energy* **2023**, *8*, 423.

(9) Hänsel, C.; Kundu, D. The Stack Pressure Dilemma in Sulfide Electrolyte Based Li Metal Solid-State Batteries: A Case Study with Li6PS5Cl Solid Electrolyte. *Adv. Mater. Interfaces* **2021**, *8*, No. 2100206.

(10) Doux, J. M.; Yang, Y.; Tan, D. H.; Nguyen, H.; Wu, E. A.; Wang, X.; Banerjee, A.; Meng, Y. S. Pressure effects on sulfide electrolytes for all solid-state batteries. *J. Mater. Chem. A* **2020**, *8*, 5049−5055.

(11) Wang, L.; Wang, X.; Yang, W. Optimal design of electric vehicle battery recycling network-From the perspective of electric vehicle manufacturers. *Appl. Energy* **2020**, *275*, No. 115328.

(12) Zhao, L.; Wang, Q. J.; Zhang, X.; Hatzell, K. B.; Zaman, W.; Martin, T. V.; Wang, Z. Laplace-Fourier transform solution to the electrochemical kinetics of a symmetric lithium cell affected by interface conformity. *J. Power Sources* **2022**, *531*, No. 231305.
(13) Tan, D. H. S.; Xu, P.; Yang, H.; Kim, M.-c.; Nguyen, H.; Wu, E. A.; Doux, J.-M.; Banerjee, A.; Meng, Y. S.; Chen, Z. Sustainable design of fully recyclable all solid-state batteries. *MRS Energy Sustainability* **2020**, *7*, 23.
(14) Doux, J. M.; Nguyen, H.; Tan, D. H.; Banerjee, A.; Wang, X.; Wu, E. A.; Jo, C.; Yang, H.; Meng, Y. S. Stack Pressure Considerations for Room-Temperature All-Solid-State Lithium Metal Batteries. *Adv. Energy Mater.* **2020**, *10*, No. 1903253.
(15) LePage, W. S.; Chen, Y.; Kazyak, E.; Chen, K.-H.; Sanchez, A. J.; Poli, A.; Arruda, E. M.; Thouless, M. D.; Dasgupta, N. P. Lithium Mechanics: Roles of Strain Rate and Temperature and Implications for Lithium Metal Batteries. *J. Electrochem. Soc.* **2019**, *166*, A89−A97.
(16) Krauskopf, T.; Hartmann, H.; Zeier, W. G.; Janek, J. Toward a Fundamental Understanding of the Lithium Metal Anode in Solid-State Batteries - An Electrochemo-Mechanical Study on the Garnet-Type Solid Electrolyte Li6.25Al0.25La3Zr2O12. *ACS Appl. Mater. Interfaces* **2019**, *11*, 14463−14477.
(17) LePage, W. S.; Chen, Y.; Kazyak, E.; Chen, K.-H.; Sanchez, A. J.; Poli, A.; Arruda, E. M.; Thouless, M.; Dasgupta, N. P. Lithium mechanics: roles of strain rate and temperature and implications for lithium metal batteries. *J. Electrochem. Soc.* **2019**, *166*, A89−A97.
(18) Lee, K.; Kazyak, E.; Wang, M. J.; Dasgupta, N. P.; Sakamoto, J. Analyzing void formation and rewetting of thin in situ-formed Li anodes on LLZO. *Joule* **2022**, *6*, 2547−2565.
(19) Zhang, X.; Wang, Q. J.; Harrison, K. L.; Jungjohann, K.; Boyce, B. L.; Roberts, S. A.; Attia, P. M.; Harris, S. J. Rethinking How External Pressure Can Suppress Dendrites in Lithium Metal Batteries. *J. Electrochem. Soc.* **2019**, *166*, A3639−A3652.
(20) Polonsky, I. A.; Keer, L. M. A numerical method for solving rough contact problems based on the multi-level multi-summation and conjugate gradient techniques. *Wear* **1999**, *231*, 206−219.
(21) Chen, W. W.; Liu, S.; Wang, Q. J. Fast Fourier transform based numerical methods for elasto-plastic contacts of nominally flat surfaces. *J. Appl. Mech., Trans. ASME* **2008**, *75*, No. 01102211.
(22) Liu, S.; Wang, Q.; Liu, G. A versatile method of discrete convolution and FFT (DC-FFT) for contact analyses. *Wear* **2000**, *243*, 101−111.
(23) Liu, S.; Wang, Q. Studying contact stress fields caused by surface tractions with a discrete convolution and fast fourier transform algorithm. *J. Tribol.* **2002**, *124*, 36−45.
(24) Han, X.; Gong, Y.; Fu, K.; He, X.; Hitz, G. T.; Dai, J.; Pearse, A.; Liu, B.; Wang, H.; Rubloff, G.; Mo, Y.; Thangadurai, V.; Wachsman, E. D.; Hu, L. Negating interfacial impedance in garnet-based solid-state Li metal batteries. *Nat. Mater.* **2017**, *16*, 572−579.
(25) Masias, A.; Felten, N.; Garcia-Mendez, R.; Wolfenstine, J.; Sakamoto, J. Elastic, plastic, and creep mechanical properties of lithium metal. *J. Mater. Sci.* **2019**, *54*, 2585−2600.
(26) Dienemann, L. L.; Saigal, A.; Zimmerman, M. A. Creep and Anisotropy of Free-Standing Lithium Metal Foils in an Industrial Dry Room. *J. Electrochem. Energy Convers. Storage* **2021**, *18*, No. 100844.
(27) Wang, M. J.; Choudhury, R.; Sakamoto, J. Characterizing the Li-Solid-Electrolyte Interface Dynamics as a Function of Stack Pressure and Current Density. *Joule* **2019**, *3*, 2165−2178.
(28) Kasemchainan, J.; Zekoll, S.; Spencer Jolly, D.; Ning, Z.; Hartley, G. O.; Marrow, J.; Bruce, P. G. Critical stripping current leads to dendrite formation on plating in lithium anode solid electrolyte cells. *Nat. Mater.* **2019**, *18*, 1105−1111.
(29) Dixit, M. B.; Verma, A.; Zaman, W.; Zhong, X.; Kenesei, P.; Park, J. S.; Almer, J.; Mukherjee, P. P.; Hatzell, K. B. Synchrotron imaging of pore formation in Li metal solid-state batteries aided by machine learning. *ACS Appl. Energy Mater.* **2020**, *3*, 9534−9542.
(30) Zhang, Z.; Chen, S.; Yao, X.; Cui, P.; Duan, J.; Luo, W.; Huang, Y.; Xu, X. Enabling high-areal-capacity all-solid-state lithium-metal batteries by tri-layer electrolyte architectures. *Energy Storage Mater.* **2020**, *24*, 714−718.
(31) Yan, H.; Tantratian, K.; Ellwood, K.; Harrison, E. T.; Nichols, M.; Cui, X.; Chen, L. How Does the Creep Stress Regulate Void Formation at the Lithium−Solid Electrolyte Interface during Stripping? *Adv. Energy Mater.* **2022**, *12* (2), 2102283.
(32) Xu, C.; Ahmad, Z.; Aryanfar, A.; Viswanathan, V.; Greer, J. R. Enhanced strength and temperature dependence of mechanical properties of Li at small scales and its implications for Li metal anodes. *Proc. Natl. Acad. Sci. U.S.A.* **2017**, *114*, 57−61.
(33) Krauskopf, T.; Mogwitz, B.; Hartmann, H.; Singh, D. K.; Zeier, W. G.; Janek, J. The Fast Charge Transfer Kinetics of the Lithium Metal Anode on the Garnet-Type Solid Electrolyte Li6.25Al0.25-La3Zr2O12. *Adv. Energy Mater.* **2020**, *10*, No. 2000945.
(34) Taylor, N. J.; Stangeland-Molo, S.; Haslam, C. G.; Sharafi, A.; Thompson, T.; Wang, M.; Garcia-Mendez, R.; Sakamoto, J. Demonstration of high current densities and extended cycling in the garnet Li7La3Zr2O12 solid electrolyte. *J. Power Sources* **2018**, *396*, 314−318.
(35) Sharafi, A.; Meyer, H. M.; Nanda, J.; Wolfenstine, J.; Sakamoto, J. Characterizing the Li-Li7La3Zr2O12 interface stability and kinetics as a function of temperature and current density. *J. Power Sources* **2016**, *302*, 135−139.
(36) Wang, M.; Wolfenstine, J. B.; Sakamoto, J. Temperature dependent flux balance of the Li/Li7La3Zr2O12 interface. *Electrochim. Acta* **2019**, *296*, 842−847.
(37) Chang, W.; May, R.; Wang, M.; Marbella, L.; Steingart, D.; Thorsteinsson, G.; Sakamoto, J. Evolving contact mechanics and microstructure formation dynamics of the lithium metal-Li7La3Zr2O12 interface. *Nat. Commun.* **2021**, *12*, No. 6369.
(38) Yang, L.; Tao, X.; Huang, X.; Zou, C.; Yi, L.; Chen, X.; Zang, Z.; Luo, Z.; Wang, X. Efficient Mutual-Compensating Li-Loss Strategy toward Highly Conductive Garnet Ceramics for Li-Metal Solid-State Batteries. *ACS Appl. Mater. Interfaces* **2021**, *13*, 56054−56063.
(39) Cheng, L.; Chen, W.; Kunz, M.; Persson, K.; Tamura, N.; Chen, G.; Doeff, M. Effect of surface microstructure on electrochemical performance of garnet solid electrolytes. *ACS Appl. Mater. Interfaces* **2015**, *7*, 2073−2081.
(40) Dussart, T.; Rividi, N.; Fialin, M.; Toussaint, G.; Stevens, P.; Laberty-Robert, C. Critical Current Density Limitation of LLZO Solid Electrolyte: Microstructure vs Interface. *J. Electrochem. Soc.* **2021**, *168*, 120550.
(41) Ma, X.; Xu, Y. Enhanced critical current density of Garnet Li7La3Zr2O12 solid electrolyte by incorporation of LiBr. *Electrochim. Acta* **2022**, *409*, No. 139986.
(42) Huang, X.; Lu, Y.; Guo, H.; Song, Z.; Xiu, T.; Badding, M. E.; Wen, Z. None-Mother-Powder Method to Prepare Dense Li-Garnet Solid Electrolytes with High Critical Current Density. *ACS Appl. Energy Mater.* **2018**, *1*, 5355−5365.
(43) Su, J.; Huang, X.; Song, Z.; Xiu, T.; Badding, M. E.; Jin, J.; Wen, Z. Overcoming the abnormal grain growth in Ga-doped Li7La3Zr2O12 to enhance the electrochemical stability against Li metal. *Ceram. Int.* **2019**, *45*, 14991−14996.
(44) Lu, Y.; Huang, X.; Ruan, Y.; Wang, Q.; Kun, R.; Wen, Z. An in situ element permeation constructed high endurance Li − LLZO interface at high current densities. *J. Mater. Chem. A* **2018**, *6*, 18853−18858.
(45) Chen, S.; Nie, Z.; Tian, F.; Nie, L.; Wei, R.; Yu, J.; Gao, T.; Sun, Z.; Yang, N.; Liu, W. The Influence of Surface Chemistry on Critical Current Density for Garnet Electrolyte. *Adv. Funct. Mater.* **2022**, *32*, No. 2113318.
(46) Mu, M.; Schmieg, J.; Dierickx, S.; Joos, J.; Weber, A.; Gerthsen, D.; Ivers-ti, E. Reducing Impedance at a Li-Metal Anode / Garnet-Type Electrolyte Interface Implementing Chemically Resolvable In Layers. *ACS Appl. Mater. Interfaces* **2022**, *2*, 14739−14752.
(47) Xu, R.; Liu, F.; Ye, Y.; Chen, H.; Yang, R. R.; Ma, Y.; Huang, W.; Wan, J.; Cui, Y. A Morphologically Stable Li/Electrolyte Interface for All-Solid-State Batteries Enabled by 3D-Micropatterned Garnet. *Adv. Mater.* **2021**, *33*, No. 2104009.
(48) Fu, Z.; Zhang, L.; Gritton, J. E.; Godbey, G.; Hamann, T.; Gong, Y.; McOwen, D.; Wachsman, E. Probing the Mechanical

Properties of a Doped Li7La3Zr2O12Garnet Thin Electrolyte for Solid-State Batteries. *ACS Appl. Mater. Interfaces* **2020**, *12*, 24693−24700.

(49) Lewis, J. A.; Lee, C.; Liu, Y.; Han, S. Y.; Prakash, D.; Klein, E. J.; Lee, H.-w.; McDowell, M. T. Role of areal capacity in determining short circuiting of sulfide-based solid-state batteries. *ACS Appl. Mater. Interfaces* **2022**, *14* (3), 4051−4060.

https://doi.org/10.1021/acsami.3c05886
ACS Appl. Mater. Interfaces 2023, 15, 37401−37409